BIOENGINEERING

Recreating the heart's helical structure-function relationship with focused rotary jet spinning

Huibin Chang[1]†, Qihan Liu[1,2]†, John F. Zimmerman[1]†, Keel Yong Lee[1], Qianru Jin[1], Michael M. Peters[1], Michael Rosnach[1], Suji Choi[1], Sean L. Kim[1], Herdeline Ann M. Ardoña[1,3], Luke A. MacQueen[1], Christophe O. Chantre[1], Sarah E. Motta[1,4], Elizabeth M. Cordoves[1], Kevin Kit Parker[1]*

Helical alignments within the heart's musculature have been speculated to be important in achieving physiological pumping efficiencies. Testing this possibility is difficult, however, because it is challenging to reproduce the fine spatial features and complex structures of the heart's musculature using current techniques. Here we report focused rotary jet spinning (FRJS), an additive manufacturing approach that enables rapid fabrication of micro/nanofiber scaffolds with programmable alignments in three-dimensional geometries. Seeding these scaffolds with cardiomyocytes enabled the biofabrication of tissue-engineered ventricles, with helically aligned models displaying more uniform deformations, greater apical shortening, and increased ejection fractions compared with circumferential alignments. The ability of FRJS to control fiber arrangements in three dimensions offers a streamlined approach to fabricating tissues and organs, with this work demonstrating how helical architectures contribute to cardiac performance.

The heart's musculature is organized in a helical fashion, with cardiomyocytes in the left ventricle smoothly transitioning transmurally from a left- to right-handed helix (1). This helical alignment results in a "wringing motion" that was first described in 1669 by Lower (2). Over the past half-century, it has been argued that this helical arrangement represents a fundamental structural design critical to achieving large ejection fractions (EFs) (1, 3–6). Although in vivo studies have proven to be a powerful tool, both in defining these structural features (7–9) and in correlating misalignments with cardiac disease and reduced ventricle function (5, 9, 10), they are often characterized by concomitant changes in protein expression and metabolism (11) and are limited by their ability to control cardiac alignments (12, 13). This makes it difficult to distinguish between biomolecular and biomechanical contributions to cardiac dysfunction. However, understanding how helical structures contribute to cardiac function is important, as some cardiomyopathies can exhibit maladaptive tissue remodeling (14, 15), which may result in more circumferential alignments of the musculature (12, 13, 15).

To study the role of helical muscular alignment on cardiac function, it is necessary to recreate the multiscale architectures of the heart, with both controlled alignments and three-dimensional (3D) geometries. In the heart, helical alignments are supported by extracellular matrix (ECM) proteins such as collagen fibrils (8, 16), the diameters of which are on the order of a single micrometer. Approaches that use 3D extrusion printing have demonstrated important milestones toward replicating such structures, including the production of microphysiological devices (17, 18), microvasculature systems (19), and spontaneously beating heart models (20, 21). However, reproducing the fine spatial features required to potentiate muscular alignment while retaining practical production rates is difficult. This is the result of a fundamental limitation in 3D extrusion printing, whereby throughput declines rapidly with respect to feature size. Consider a full-size human heart. Printing the ECM components at current resolutions (~250 μm feature sizes) takes hours to days (22), but at native feature sizes (1 μm) could take hundreds of years if current scaling trends are followed (eq. S1). Because fiber-spinning techniques can reproduce these fine spatial features with higher throughputs, they offer a potential solution and have been used previously to engineer tissue scaffolds, such as heart valves (23) and ventricle models (24). However, unlike 3D printing, fiber-spinning approaches often fail to recreate complex 3D geometries while maintaining controlled alignments.

We developed focused rotary jet spinning (FRJS), an additive manufacturing method that uses centrifugal jet spinning to rapidly form polymeric micro/nanofibers, which are then focused and spatially patterned by means of a controlled airstream. This approach allows for the rapid manufacturing of fiber constructs with programmable fiber alignments in three dimensions. Because fibers can be used to direct tissue formation, it is possible to recreate complex anatomies that were hitherto unobtainable via current biofabrication techniques. Basing our study on Sallin's analytical model of the heart (3), we used FRJS to manufacture both helically aligned (HA) and circumferentially aligned (CA) tissue-engineered models of the left ventricle, showing that the biomechanics of these single-layer ventricle models is consistent with theoretical predictions from the past 50 years (3, 4, 25). Collectively, this work reveals how a FRJS-based approach to biofabrication can be used to rapidly create robust model organs, with increased geometric complexity.

Fiber manufacture using focused rotary jet spinning

Methods such as electrospinning (26), melt blowing (27), pull spinning (28), and traditional centrifugal spinning (29) can form micro/nanofibers. When producing single-micrometer features, these techniques can offer orders of magnitude greater throughputs than those achieved by 3D extrusion printing (30). However, fiber-spinning methods are often less precise, failing to accurately recreate complex 3D geometries and alignments. This lack of precision is partly because fiber formation and patterning are traditionally interrelated during fiber production. In FRJS, decoupling the fiber formation and patterning processes is realized by creating a focused stream of preformed fibers (Fig. 1, A to C; fig. S1, and movie S1). Rotary jet spinning produces fibers by centrifugal force, pushing polymer solutions through a small orifice in the spinneret. Subsequent jet elongation results in free-floating single-micrometer fibers (29). This allows for a formation period that is independent of fiber patterning, generating a cloud of fibers that surrounds the spinneret. Next, in a phenomenon known as entrainment (31), fibers are pulled into a jet stream blown from the center of the spinneret. Because air speeds are orders of magnitude slower outside of the jet (fig. S2), this entrainment process minimally perturbs fiber formation (fig. S3). The jet stream then allows for fibers to become aligned and confined in a small region, focusing them for patterning.

Focusing the fibers in this manner enables them to be conformally deposited, meaning that fibers will adhere well to convex structures or features with curvature radii that exceed the focal spot size (fig. S4). To demonstrate this focusing effect in FRJS, polycaprolactone fibers were collected at regular intervals from within the airstream to measure deposition profiles. This showed that, at the narrowest point, 95% of fiber deposition occurred within a spot size of 5.0 ± 0.3 cm (2σ of Gaussian distribution) (Fig. 1B, ii, and fig. S4). To demonstrate conformal deposition, fibers were then spun onto both a rotating collection mandrel (movie S2) and a 1-cm ventricle model

[1]Disease Biophysics Group, John A. Paulson School of Engineering and Applied Science, Harvard University, Boston, MA 02134, USA. [2]Department of Mechanical Engineering and Materials Science, University of Pittsburgh, Pittsburgh, PA 15261, USA. [3]Department of Chemical and Biomolecular Engineering, Samueli School of Engineering, University of California, Irvine, CA 92697, USA. [4]Institute for Regenerative Medicine, University of Zurich, Zurich, Switzerland.
*Corresponding author. Email: kkparker@seas.harvard.edu
†These authors contributed equally to this work.

Fig. 1. Focused rotary jet spinning for producing helical structures. (**A**) Schematic diagram of the helical alignment of a human heart. (**B** and **C**) FRJS uses focused air to separate fiber manufacture into formation (B, i) and patterning (C) phases, allowing for controlled alignments during deposition. (B, ii) Differential contrast projection of the fiber stream (maximal projection; scale bar, 5 cm). (**D**) Image of polycaprolactone spun onto a mandrel (scale bar, 5 mm), with corresponding scanning electron microscopy (SEM) image, showing aligned fiber formation (mean fiber diameter, ~900 nm; scale bar, 5 μm). (**E**) Schematic diagram showing that collection angle (θ) dictates fiber deposition alignment (i), with OOP indicating the relative average alignment (error bars, mean ± SD) (ii). SEM micrographs (iii to v; 0°, 60°, and 90°, respectively) with corresponding 2D Fourier transforms inset, indicating that the degree of alignment is based on collection angle (scale bars, 5 μm). (**F**) Schematic diagram showing HA fiber manufacture based on angle (i), α, with a representative fiber-coated rod (ii) and reconstructed micro–computed tomograph of a HA scaffold (iii; scale bar, 200 μm).
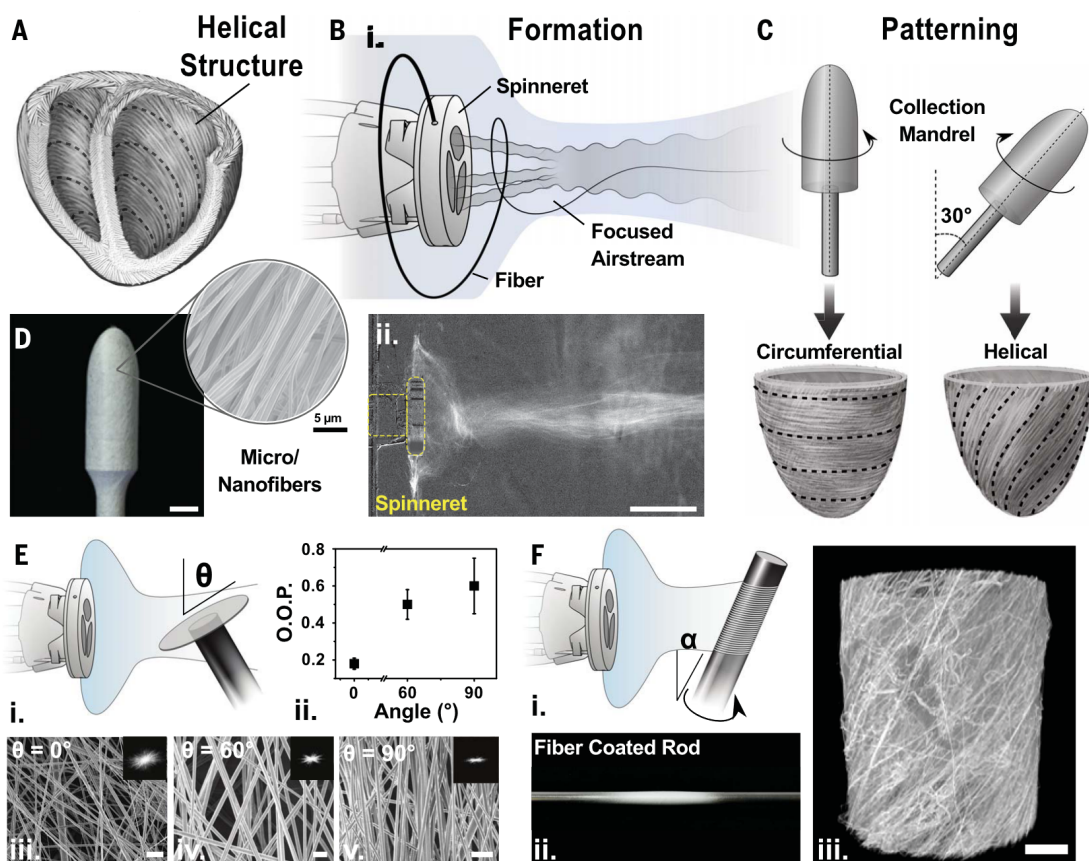
(Fig. 1D). In each case, targets were coated in ~5 min, forming standalone structures that could be removed and manipulated. Additionally, we showed that this approach could be used with a variety of material compositions, such as nylon, polyurethane, and gelatin, while maintaining single-micrometer fiber diameters (fig. S5).

Controlled distribution of fiber alignment

Envisioning that micro/nanofibers could mimic the structural features of ECM proteins, we examined how FRJS could be used to control the anisotropic distribution of fiber alignments. We hypothesized that the alignment of fibers in the air stream could enable controlled deposition, in which tangential collection (θ = 0°) should minimally perturb airflow, while head-on deposition (θ = 90°) would enable divergent patterning. To test this hypothesis, the collector angle relative to the fiber stream was modulated during deposition (Fig. 1E), with the orientation order parameter (OOP) used as a metric of subsequent fiber organization (32). The resulting fibers displayed angle-dependent anisotropy, with tangential, intermediate, and perpendicular collection leading to highly anisotropic (θ = 0°, OOP = 0.60 ± 0.15), intermediate (θ = 60°, OOP = 0.50 ± 0.08),

and randomly aligned (θ = 90°, OOP = 0.18 ± 0.03) fiber distributions, respectively.

This ability to control fiber orientation suggested that more complex patterning could be achieved by moving the target relative to the stream. To test whether FRJS could recreate key geometric features of the heart, such as the helical alignments and laminar tissue structures identified in a rodent model (fig. S6, A and B), fibers were collected on an inclined rotating cylinder to generate helical alignments (Fig. 1F and movie S3) and on an incrementally rotating disk to generate multilayered fiber sheets (fig. S6C and movie S4). We observed that FRJS was able to accurately reproduce these structures, as confirmed by x-ray micro–computed tomography (μCT). This suggested that FRJS could be effectively employed in hierarchical biofabrication, in which the focused air stream provides gross structural morphology (centimeter scale), whereas fibers provide fine structural (single-micrometer scale) cues to promote tissue morphogenesis.

## Building helically aligned models of the left ventricle

We reasoned that the ability of FRJS to control fiber alignment could be used to test Sallin's

hypothesis (3) and the advantages of helically versus circumferentially aligned ventricular geometries. Basing our experimental approach Sallin's analytical model of the heart (3), we then used FRJS to produce both CA (α = 0°) and HA (α = 30°) (60° with respect to the ventricle's long axis) single-layer models of the left ventricle (Fig. 2A). HA fiber orientations were selected on the basis of energy minimization constraints, with angles between 20° and 45° predicted to be the most energy efficient for pumping fluids (4). Fiber scaffolds were designed to have mechanical properties consistent with those of human heart tissues (fig. S7 and table S2).

After fiber manufacture, gelatin fiber scaffolds were then seeded with either primary neonatal rat ventricular myocytes (NRVMs) or human induced pluripotent stem cell–derived cardiomyocytes (hiPSC-CMs), resulting in confluent tissues with depths between one to three layers of cardiomyocytes (fig. S8). hiPSC-CMs were differentiated in vitro for 15 days total before seeding, forming visible spontaneous contractions after 7 days and staining positive for sarcomeric α-actinin (fig. S9). To ensure that FRJS fiber spinning could be used to direct tissue alignment, we first examined NRVMs seeded onto laminar

Fig. 2. Tissue scaffolds with controlled helical alignments.
(**A**) Bright-field micrograph of a HA ventricle model (gelatin fibers seeded with NRVMs; scale bar, 2 mm). (**B**) SEM micrograph of fibers from CA [(i), α = 0°] and HA [(iii), α = 45°] cylinders, with corresponding immunofluorescent staining of cardiomyocytes (ii and iv) [NRVM; blue, DAPI (4′,6-diamidino-2-phenylindole); green, f-actin; red, sarcomeres], showing that fibers help direct tissue alignment (scale bars, 50 μm). Circ., circumferential. (**C**) Iso-chrones (top) with corresponding still frames (bottom), indicating calcium transience along an extended ventricle surface, showing increased transverse wave propagation for HA scaffolds. Tissues were point-stimulated apically [(i), CA; (ii), HA] (scale bars, 5 mm). (**D**) Schematic diagram of a CA (left) and HA (right) ventricle, illustrating differences in wall displacement during contraction. CA contracts as concentric rings, whereas HA follows a wringing motion, resulting in different predicted EFs [k, strain, q, apical shortening, $H(α)$, radial shortening]. (**E**) Deformation maps generated by CA (left) and HA (right) ventricle models during contraction (scale bar, 2 mm).

In schematic (D):
$$EF(k) = 1 - k^2$$
$$EF(k, q, α) = 1 - k^2 \cdot q \cdot H(α)$$
$$q \leq 1 \quad H(α) \leq 1$$
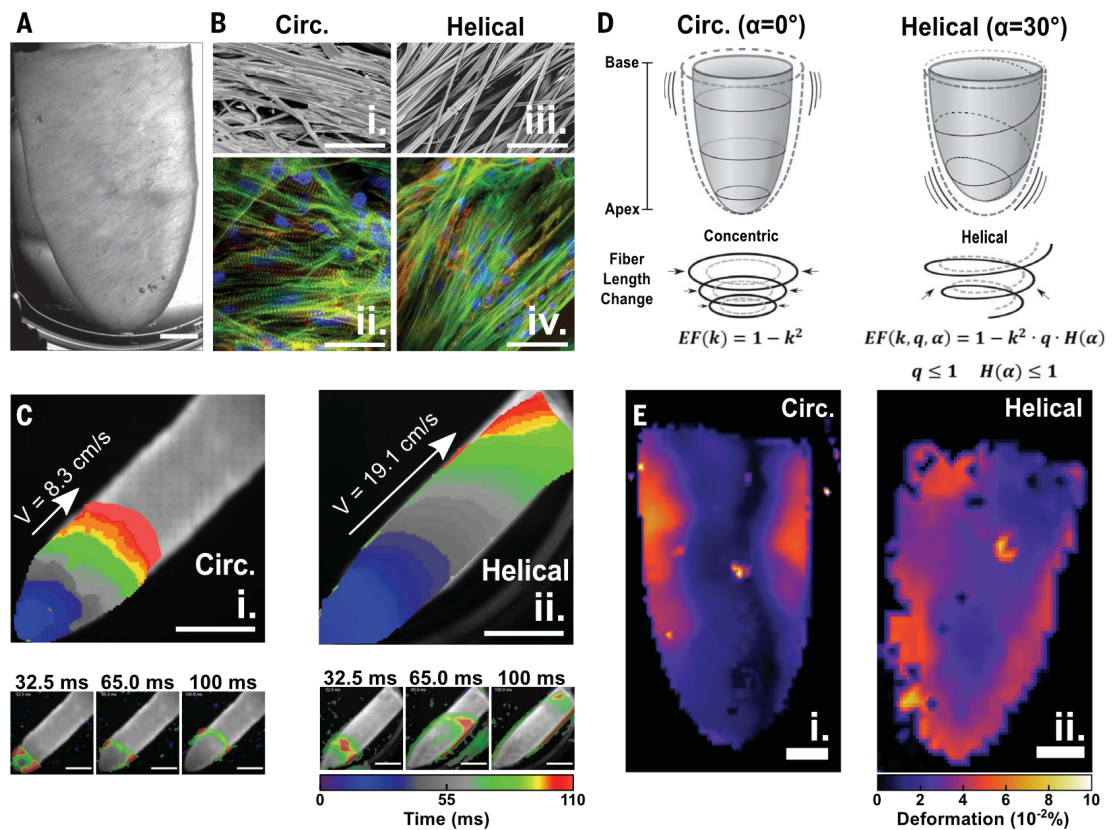
tissue constructs. This resulted in tissues with a highly anisotropic distribution and cell alignment that conformed to the underlying fiber orientation (Fig. 2B and fig. S10). Next, after seeding 3D scaffolds with either NRVMs (movie S5) or hiPSC-CMs (movie S6), spontaneous contractions were observed after 3 to 5 days. These data demonstrate that FRJS could be used to form 3D contractile cardiac models.

Calcium wave propagation

To demonstrate syncytium formation, we examined the ability of the model ventricles to sustain uniform calcium wave propagation. In healthy tissues, action potentials propagate faster in the direction of cell alignment, with myocytes showing slower conduction velocities (CVs) in the transverse direction (33). Given this insight, we reasoned that electrical signal propagation should vary depending on the ventricle's fiber alignment and could be used to confirm long-range tissue formation and directional alignment in these model systems. To measure directional signal conduction in tissue scaffolds, laminar tissues were electrically stimulated (corner point stimulation), and the resulting calcium propagation was measured with an optical mapping system (fig. S11). We observed higher CVs in the direction of fiber alignment [longitudinal CVs (LCVs)] with re-spect to transverse CVs (TCVs), with LCVs and TCVs of 14.9 ± 5.8 cm/s and 9.0 ± 3.7 cm/s, respectively (n = 9 samples) at ratios of ~1.5 to 2.0. These values were consistent with previous reports of in vitro tissues composed of immature cardiomyocytes, where factors such as geometry, calcium handling, and gap junction expression can influence CV (24, 34, 35). Turning to 3D models, ventricles with extended basal regions, allowing for increased travel distances, were apically stimulated. Isochrones of the calcium propagation revealed that CA scaffolds displayed only modest CVs (8.3 cm/s) along the ventricle's long axis, whereas HA ventricles showed increased CVs (19.1 cm/s) with respect to CA ventricles (Fig. 2C and movie S7). Together, these findings demonstrated that our tissues maintained their alignment and confluence over the length of the ventricle (~1 cm) and further suggested the importance of cardiomyocyte alignment in regulating the spatiotemporal control of excitation-contraction coupling.
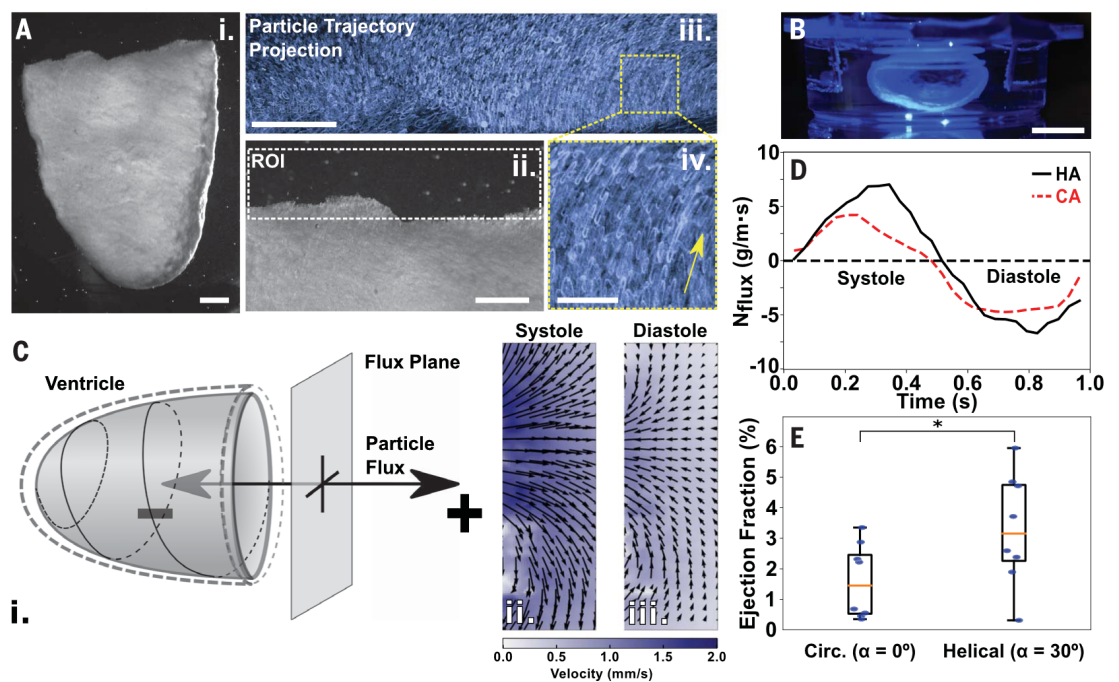
Ventricular deformation

It has been hypothesized that HA ventricles would display increased apical shortening (3, 36) and reduced basal displacement (9, 36), owing to differences in myofiber lengths. Because cardiomyocytes contract along their long axis during systole, while connecting transversely as a bulk material (37), they generate forces primarily along the length of the fibers. This means that longer fibers should result in greater total displacements. For CA ventricles, which are made up of concentric rings, fiber length is greatest at the base, where the radius is largest, and smallest at the apex (Fig. 2D). This should result in nonuniform deformations, with greater displacements in the basal region and negligible displacements at the apex. For HA ventricles, however, fiber length should vary minimally, as fibers extend uniformly from the apex to the base of the ventricle. Overall, this should result in more homogenous deformations for HA ventricles, with increased apical shortening.

Examining how CA and HA models deformed during contraction, we visualized displacement by submerging these ventricles into a solution containing nonspecifically adherent fluorescent beads. Using digital image cross-correlation, we performed deformation mapping across the ventricle's surface during 1-Hz field stimulation (movie S8). As predicted, CA ventricles displayed greater deformations near the base of the ventricle, whereas HA scaffolds showed more-uniform deformations (Fig. 2E). Probing further, we measured changes in the boundary shape using an elliptical fit, indicating substantial differences in deformation

Fig. 3. Alignment dictates ventricular ejection fractions.
(**A**) (i) Bright-field micrograph of a tissue-engineered ventricle, with (ii) a magnified view of the ventricular basal region. ROI, region of interest. (iii) Maximum intensity projection of fluorescent beads taken over a single contraction cycle, showing particle displacement. (iv) High-magnification image of the boxed region in (iii); the arrow indicates the direction of fluid displacement [scale bars in (i) to (iii), 2 mm; in (iv), 0.5 mm]. (**B**) Side view of the ventricle (scale bar, 10 mm). (**C**) (i) Schematic diagram of PIV measurement, with velocity fields [(ii) and (iii)] taken from the base of a HA ventricle scaffold during peak systole [(ii), $t = 0.3$ s] and diastole [(iii), $t = 0.7$ s]. (**D**) Representative measurements of the instantaneous mass flux (N_{flux}) in the region of interest as function of contraction time and ventricle angle. (**E**) Ensemble measurements of EF for CA and HA ventricle scaffolds ($n = 8$ ventricles for each angle; *$P < 0.05$ by Student's t test; box plot given in quartiles).

between each alignment. CA samples showed greater basal and minimal longitudinal constriction, whereas HA ventricles displayed significant apical shortening with reduced basal deformation ($n \geq 5$ ventricles for each condition) (fig. S12). Overall, these results were consistent with the projections of previous analytical and computational models (*3*, *25*, *36*) in that they showed more-homogeneous deformations for HA ventricles.

These changes in ventricular contraction were also suggestive of further functional differences between myofiber alignments. For instance, apical shortening indicated the potential for a wringing motion or ventricle twist to occur in HA ventricles. Additionally, this suggested the possibility for variable EFs on the basis of fiber alignment, as these differences in deformation could result in distinct volumetric displacements. It has been predicted that EFs should scale as $1 - k^2$ for CA ventricles (eq. S5) and $1 - k^2 \cdot q \cdot H(\alpha)$ for HA ventricles (eq. S15) (Fig. 2D) (*3*), with k being the strain along the fiber axis, q being the apical shortening, and $H(\alpha)$ being the radial shortening based on the fiber's helical angle (eqs. S5 to S15). q and $H(\alpha)$ are defined as ≤1, which suggests that HA ventricles could produce larger EFs.

Ventricular twist

To determine whether ventricular twist was preserved in our model system, we measured rotational displacement at the apex of suspended ventricle scaffolds (fig. S13, A to B).

In a healthy heart, kinetic energy is stored during contraction in the sarcomeric protein titin and is subsequently released during relaxation (*38*), giving rise to rotational displacements, or ventricular twist (*1*, *38*). HA and CA scaffolds were sutured at the base to a fixed support, allowing the apex to move freely, and were monitored from below during field stimulation. Using edge features to detect rotation (fig. S13, C to E), we observed that CA scaffolds showed minimal twist ($1.35 \pm 1.1°$, $n = 7$ ventricles). Conversely, HA scaffolds displayed approximately four times as much twist ($5.4 \pm 3.6°$, $n = 7$ ventricles) (movie S9), modeling physiological ventricular twist in an in vitro system.

## Cardiac output and ejection fractions

To determine whether these structural changes in alignment and deformation lead to altered function, we then used cardiac output (CO) and EF as quantitative metrics of cardiac performance. To measure these values, we first used catheterization to monitor pressure-volume changes in the ventricle scaffolds, observing the formation of complete oblate loops (fig. S14). However, submerged gelatin fibers are a poor dielectric, making it difficult to obtain consistent results in our synthetic scaffolds by means of conductance catheterization. Consequently, particle imaging velocimetry (PIV) was used to further quantify cardiac performance.

Model ventricles were suspended in a bath containing neutrally buoyant fluorescent beads, and bead displacement was tracked. This al-

lowed for the construction of 2D velocity fields surrounding the basal opening, as shown for a HA ventricle model (Fig. 3, A and B). Using PIV, we then evaluated the instantaneous mass flux resulting from ventricle contraction (fig. S15 and movie S10) and observed cyclic outputs, with fluid being expelled during systole and refill occurring during diastole (Fig. 3, C and D). This was performed for ventricles with both varying fiber alignments and fibroblast compositions (fig. S16). Summation of the fluid displacement over systole yields the total CO, with values of 11.7 ± 8.9 μl/s and 24.3 ± 13.5 μl/s ($n = 8$ samples each) for CA and HA ventricle scaffolds, respectively (fig. S15G). This observation represented a significant ($P < 0.05$) CO increase based purely on ventricular tissue alignment. Normalizing the CO by diastolic ventricle volume and fluid density, we calculated the resulting EFs. This yielded average EFs of $1.6 \pm 1.1\%$ and $3.3 \pm 1.7\%$ in the CA and HA case, respectively ($n = 8$ samples each), with a maximum EF of 5.9% observed in the helical case (Fig. 3E). This indicated that helical alignments confer a relative increase in ventricle output. To compare our findings with Sallin's analytical model of ventricle contraction (*3*), we then normalized our results on the basis of relative contractile strain (eqs. S5 to S15). Sallin's model predicted an EF increase of 54 to 64% for HA ventricles, which was consistent with our experimental observations (within the standard error of the mean; Fig. 3E). This indicated that our model system was capable of preserving these fundamental scaling laws, signifying that helical

Fig. 4. Multiscale heart models.
(**A**) Simplified design of a trilayered DCV that mimics the native ECM alignment of the heart, highlighting the four-step manufacturing process.
(**B**) (i) µCT imaging of the DCV suspended on the collection mandrel, with corresponding coronal cross sections (ii) (scale bars, 5 mm). (iii to v) High-magnification µCT images taken from the intraventricular septum (highlighted in purple), showing trilayer alignments (scale bars, 25 µm). RV, right ventricle; LV, left ventricle. (**C**) DCV in culture seeded with NRVMs, as viewed from the side [(i), coronal] and looking into the two chambers [(ii), transverse]. (**D**) 3D extrusion printing scales as a power law with respect to feature size, showing that the throughput of FRJS is ~10^6 times greater than that of 3D extrusion printing for single-micrometer features.

Dual Chamber Ventricle

Micro Computed Tomography (µCT)

Full-Scale Fiber Heart Model

(**E**) Left ventricle width for different species. (i to iv) Single-layer ventricles of different sizes, which can be rapidly manufactured owing to increased fiber production rates, while maintaining a single-micrometer feature scale [scale bars (left to right), 5 mm; 15 mm; 4 cm; and 8 cm]. (**F**) Full-scale four-chambered human heart model composed of single-micrometer fibers (scale bar, 2 cm).
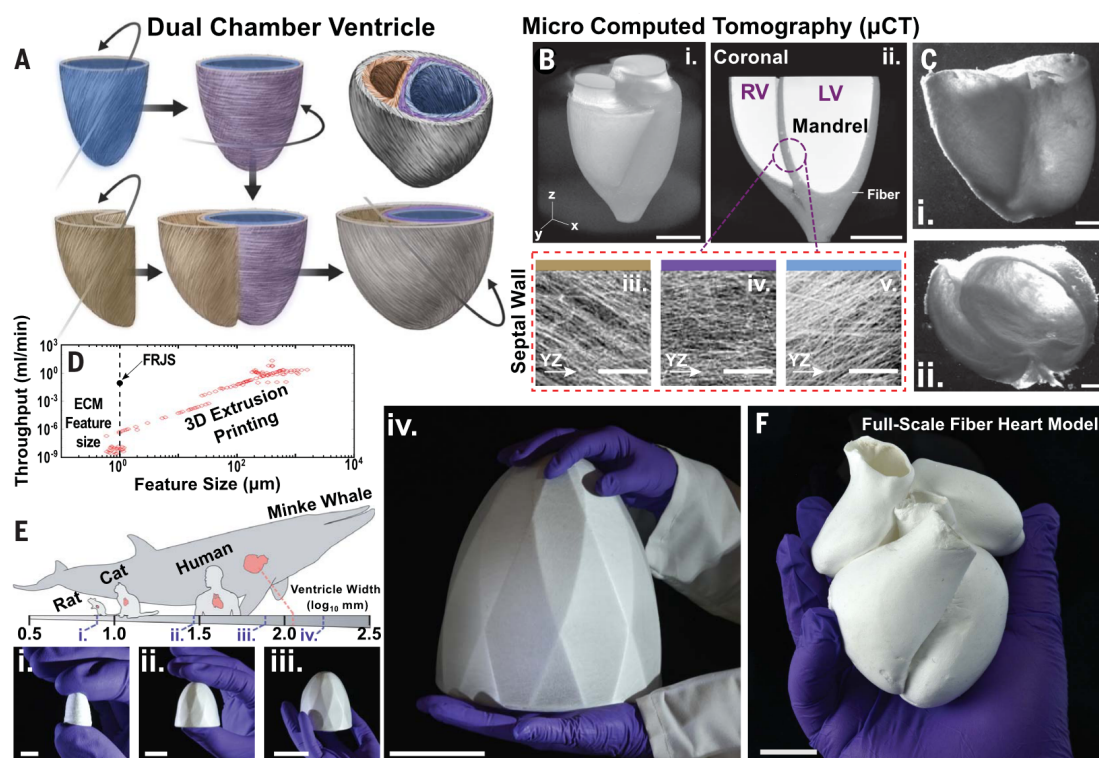
alignments of the ventricular myocardium result in increased EFs.

Dual-chambered ventricles and full-scale heart models

Scaling Sallin's model to physiological relevant strains (~15 to 20%) (3), we noted that single-angle ventricles could achieve EFs of only up to ~43% (α = 30°) (see supplementary materials for details). This EF is comparable to values experienced during borderline heart failure and underscores the importance of multiple helical alignments in maintaining healthy cardiac function. To examine whether we could mimic these architectures using FRJS, we manufactured both a dual-chambered ventricle (DCV) with multiple helical angles and a full-scale human heart model (Fig. 4). DCVs were fabricated using a multistage process, creating inner and outer helical layers, with an intermediate circumferential sheet reminiscent of the native myocardium (fig. S17, Fig. 4, A and B, and movie S11). These competing helical structures were confirmed with µCT, indicating three distinct transmural layers along the septal wall (Fig. 4B and movies S12 and S13). DCVs were then seeded with either hiPSC-CMs or NRVMs, forming contractile tissue constructs (Fig. 4C, fig. S18A, and movies S14 to S15). Examining excised segments of the left ventricle, cultured with hiPSC-CMs, we observed that cells adhered to the fibers, forming

aligned tissues (fig. S18B). Additionally, calcium imaging revealed sustained wave propagation across the ventricle surface, primarily in the direction of fiber alignment, indicating the formation of a continuous cardiac syncytium (n ≥3 samples for each condition) (fig. S18, C and D). Overall, these observations indicated that fiber scaffolds can also support human stem cell–derived tissues in complex geometries.

We then spun fibers onto ventricle-shaped targets of varying size, ranging from ~1 to 20 cm in diameter (fig. S19 and movie S16). In each case, targets were coated in <35 min with micro/nanofibers, generating conformal coatings on the exterior. Throughout this process, fibers were produced with a total throughput rate of 0.1 g/min, or 0.03 ghm (grams per hole per minute). This throughput is comparable to those of melt-blowing processes (27) but is orders of magnitude greater (~10^6) than that of 3D extrusion printing, the speed of which declines rapidly at single-micrometer features (as a power law, with a scaling factor of ~2.8) (Fig. 4, D and E, and eq. S1). Collectively, these observations demonstrated that FRJS is amenable to rapidly manufacturing fiber scaffolds spanning multiple length scales and can be adapted to different geometries.

To demonstrate the ability of FRJS to enable hierarchical biofabrication, a full-size model of the human heart musculature was constructed. This model was assembled by individually pat-

terning micro/nanofibers onto dissolvable collectors in the shape of each of the heart's four chambers (fig. S20). Individual chambers were then connected by chemical annealing before the interior supports were dissolved, resulting in standalone fiber scaffolds (Fig. 4F). Although full-size anatomical models have previously been produced with thermoplastics and hydrogels (22), these systems typically lack the micrometer-scale features needed to direct myocyte alignment. With our fiber-based approach, these local structures can be preserved across entire tissue volumes, allowing for the hierarchical assembly of tissues. These proof-of-concept 3D organ models demonstrate that FRJS scaffolds support human-derived tissues and allow for rapid assembly of full-size models of the musculature. These key features mark fiber-based manufacturing as a promising approach for achieving whole-organ biofabrication, which can be used as an alternative to or in conjunction with emerging biomanufacturing platforms such as 3D extrusion printing.

Discussion

Biofabrication using FRJS allowed for the rapid assembly of functional 3D ventricle models capable of recapitulating emergent phenomena in vitro, including ventricular twist, strain displacement, and myocardial angle-dependent EFs. Although the metrics presented

here (e.g., EF) were greater (by a factor of ~3) than for recently reported in vitro ventricle models (*24*, *39*), they were still substantially lower than in vivo values (tables S2 and S3). This difference may be the result of limited cardiomyocyte penetration into the fiber scaffolds (figs. S7 and S8). Consequently, further work is needed to achieve full-scale de novo organ fabrication; this includes improved cardiac maturation, vascularization, and incorporating consistent back-pressures (Frank-Starling mechanism). There is also a need to generate the large numbers of cardiomyocytes and other diverse cell populations (e.g., neurons, endothelial cells, fibroblasts) required to support organ biofabrication. However, the work presented here provides an initial pathway toward achieving hierarchical patterning while maintaining 3D cell alignment.

In addition to biofabrication, FRJS may serve an important role in other additive manufacturing applications, as it provides production rates comparable to those of current industrial processes while enabling micro/nanoscale feature sizes and controlled 3D alignments. This includes applications in which a material's properties are determined by its microstructure and alignment. The high surface area–to–volume ratio of micro- and nanofibers makes them ideal candidates for the controlled absorbance and release of chemical species. This suggests that FRJS may be an important technique for industrial manufacturing process that use hierarchical design principles, for which control over several orders of spatial magnitude is needed.

REFERENCES AND NOTES

1. P. P. Sengupta, A. J. Tajik, K. Chandrasekaran, B. K. Khandheria, *JACC Cardiovasc. Imaging* **1**, 366–376 (2008).
2. R. Lower, *Tractatus de Corde. Item de Motu & Colore Sanguinis et Chyli in eum Transitu* (Allestry, 1669); available at https://www.woodlibrarymuseum.org/rare-book/lower-r-tractatus-de-corde-item-de-motu-colore-sanguinis-et-chyli-in-eum-transitu-1669/.
3. E. A. Sallin, *Biophys. J.* **9**, 954–964 (1969).
4. A. Grosberg, M. Gharib, A. Kheradvar, *Bull. Math. Biol.* **71**, 1580–1598 (2009).
5. J. S. Davis *et al.*, *Cell* **107**, 631–641 (2001).
6. R. S. Stephenson *et al.*, *Clin. Anat.* **29**, 316–332 (2016).
7. P. Agger, R. S. Stephenson, *J. Cardiovasc. Dev. Dis.* **7**, 47 (2020).
8. K. D. Costa, Y. Takayama, A. D. McCulloch, J. W. Covell, *Am. J. Physiol.* **276**, H595–H607 (1999).
9. E. D. Carruth, A. D. McCulloch, J. H. Omens, *Prog. Biophys. Mol. Biol.* **122**, 215–226 (2016).
10. S. Puwanant *et al.*, *Circulation* **121**, 259–266 (2010).
11. J. Zhang, *Clin. Exp. Pharmacol. Physiol.* **29**, 351–359 (2002).
12. P. Agger *et al.*, *J. Cardiovasc. Magn. Reson.* **19**, 93 (2017).
13. E. D. Carruth *et al.*, *J. Cardiovasc. Magn. Reson.* **22**, 21 (2020).
14. M. L. McCain, S. P. Sheehy, A. Grosberg, J. A. Goss, K. K. Parker, *Proc. Natl. Acad. Sci. U.S.A.* **110**, 9770–9775 (2013).
15. C. L. Hung *et al.*, *J. Am. Coll. Cardiol.* **56**, 1812–1822 (2010).
16. J. B. Caulfield, T. K. Borg, *Lab. Invest.* **40**, 364–372 (1979).
17. J. U. Lind *et al.*, *Nat. Mater.* **16**, 303–308 (2017).
18. F. B. Coulter *et al.*, *Matter* **1**, 266–279 (2019).
19. M. A. Skylar-Scott *et al.*, *Sci. Adv.* **5**, eaaw2459 (2019).
20. A. Lee *et al.*, *Science* **365**, 482–487 (2019).
21. N. Noor *et al.*, *Adv. Sci.* **6**, 1900344 (2019).
22. E. Mirdamadi, J. W. Tashman, D. J. Shiwarski, R. N. Palchesko, A. W. Feinberg, *ACS Biomater. Sci. Eng.* **6**, 6453–6459 (2020).
23. A. K. Capulli *et al.*, *Biomaterials* **133**, 229–241 (2017).
24. L. A. MacQueen *et al.*, *Nat. Biomed. Eng.* **2**, 930–941 (2018).
25. B. Baillargeon, N. Rebelo, D. D. Fox, R. L. Taylor, E. Kuhl, *Eur. J. Mech. A* **48**, 38–47 (2014).
26. D. Li, Y. Xia, *Adv. Mater.* **16**, 1151–1170 (2004).
27. Y. Kara, K. Molnár, *J. Ind. Text.* 10.1177/15280837211019488 (2021).
28. L. F. Deravi *et al.*, *Macromol. Mater. Eng.* **302**, 1600404 (2017).
29. M. R. Badrossamay, H. A. McIlwee, J. A. Goss, K. K. Parker, *Nano Lett.* **10**, 2257–2261 (2010).
30. J. Go, S. N. Schiffres, A. G. Stevens, A. J. Hart, *Addit. Manuf.* **16**, 1–11 (2017).
31. P. Davidson, *Turbulence: An Introduction for Scientists and Engineers* (Oxford Univ. Press, 2015).
32. F. S. Pasqualini, S. P. Sheehy, A. Agarwal, Y. Aratyn-Schaus, K. K. Parker, *Stem Cell Rep.* **4**, 340–347 (2015).
33. M. Valderrábano, *Prog. Biophys. Mol. Biol.* **94**, 144–168 (2007).
34. S. Rohr, J. P. Kucera, A. G. Kléber, *Circ. Res.* **83**, 781–794 (1998).
35. A. G. Kléber, Q. Jin, *Biophys. Rev.* **2**, 031301 (2021).
36. N. B. Ingels Jr., *Technol. Health Care* **5**, 45–52 (1997).
37. R. H. Anderson, P. F. Niederer, D. Sanchez-Quintana, R. S. Stephenson, P. Agger, *J. Anat.* **235**, 697–705 (2019).
38. A. M. S. Omar, S. Vallabhajosyula, P. P. Sengupta, *Circ. Cardiovasc. Imaging* **8**, e003029 (2015).
39. M. E. Kupfer *et al.*, *Circ. Res.* **127**, 207–224 (2020).
40. SeasDBG, SeasDBG/FRJS: Recreating the Heart's Helical Structure-Function Relationship with Focused Rotary Jet Spinning- Data Analysis, *Zenodo* (2022); https://doi.org/10.5281/zenodo.6547775.

SUPPLEMENTARY MATERIALS

science.org/doi/10.1126/science.abl6395
Materials and Methods
Figs. S1 to S20
Tables S1 to S3
References (*41–54*)
MDAR Reproducibility Checklist
Movies S1 to S16

Submitted 26 July 2021; resubmitted 1 April 2022
Accepted 16 May 2022
10.1126/science.abl6395